Journal of Geophysical Research: Atmospheres

RESEARCH ARTICLE
10.1029/2018JD028934

Hurricane Warm-Core Retrievals from AMSU-A and Remapped ATMS Measurements with Rain Contamination Eliminated

Xiaolei Zou[1] and Xiaoxu Tian[1]

[1]Earth Science System Interdisciplinary Center, University of Maryland, College Park, MD, USA

Key Points:
- A remapping algorithm is applied to obtain AMSU-A-like ATMS fields of view
- A rainband-like artificial warm-core structure is caused by rain contamination in ATMS channels 5–7
- Impacts of rain contamination on the warm-core retrieval results in the low troposphere and rainy areas are removed

Correspondence to:
X. Zou,
xzou1@umd.edu

Citation:
Zou, X., & Tian, X. (2018). Hurricane warm-core retrievals from AMSU-A and remapped ATMS measurements with rain contamination eliminated. *Journal of Geophysical Research: Atmospheres*, *123*, 10,815–10,829. https://doi.org/10.1029/2018JD028934

Received 2 MAY 2018
Accepted 17 AUG 2018
Accepted article online 30 AUG 2018
Published online 2 OCT 2018

Abstract Due to a shorter effective integration time for each field of view of the Advanced Microwave Temperature Sounder (ATMS) onboard the Suomi National Polar-orbiting Partnership (S-NPP) satellite than that for the Advanced Microwave Sounding Unit-A (AMSU-A) onboard previous National Oceanic and Atmospheric Administration (NOAA) polar-orbiting satellites NOAA-15 to NOAA-19, ATMS temperature-sounding channels have higher observational resolutions and larger noise equivalent differential temperatures than the corresponding AMSU-A channels. The high resolution of the ATMS allows hurricane rainband features that are not resolvable by AMSU-A to be captured. But the larger noise equivalent differential temperature of ATMS weakens this capability through the significant impact of observational noise on warm-core retrievals. In this study, a remapping algorithm is applied to obtain AMSU-A-like ATMS fields of view to suppress this noise. A modified warm-core retrieval algorithm, which consists of two sets of training coefficients for clear-sky and cloudy conditions, is applied to limb-corrected ATMS and AMSU-A measurements using collocated Global Positioning System radio occultation observations in the previous month of the targeted hurricanes as training data sets. ATMS channels 5, 6, and 7 (AMSU-A channels 4, 5, and 6) are excluded when training the coefficients for cloudy conditions to avoid cloud/rain contamination. As a result, the abnormal cold core in the low and middle troposphere and the banded warm structures in phase with rainbands are both successfully removed. The warm-core evolution of Hurricane Matthew (2016) during its entire life span is temporally consistent on intensity as obtained from NOAA-15, NOAA-18, and MetOp-B AMSU-A observations and S-NPP ATMS observations.

1. Introduction

Hurricane centers are warmer than their environments by more than several degrees and are often called warm-core cyclones. An adiabatic warming of the atmosphere with a downward motion at the eye and the associated latent heat release, and precipitation near and outside of the eye wall all contribute to the formation of hurricane warm-cores. A subsidence warming induced by convective bursts during the onset of rapid intensification also contributes to the formation and/or intensification of warm-cores in the upper troposphere (Chen & Zhang, 2013). La Seur and Hawkins (1963), Hawking and Rubsam (1968), and Hawkins and Imbembo (1976) examined reconnaissance aircraft data and found that warm-cores were located around 250 hPa in the temperature field, which was reconstructed using aircraft reconnaissance data at the 500- and 180-hPa pressure levels. Halverson et al. (2006) used dropsonde observations to find that the primary warm-core of Hurricane Erin (2001) was near 500 hPa. Durden (2013) generated composites of in situ observations (buoys, measuring instruments mounted on ships and aircraft, dropsondes, and weather stations on islands) and confirmed that warm-core heights vary between 760 and 250 hPa. Through idealized model simulations, Stern and Nolan (2012) concluded that primary warm-cores having maximum warm anomalies are located within the 4–8 km (~700–150 hPa) vertical layer of the atmosphere. Although the exact altitudes of the maximum centers of warm-cores vary from case to case, their intensities (the warm-core anomalies) are positively correlated to hurricane intensities (Komaromi & Doyle, 2017). An early detection of warm-core formation could also provide insights on the formation of hurricanes from tropical depressions (Dolling & Barnes, 2012).

In comparison with conventional in situ observations, satellite remote sensing observations are advantageous in their horizontal, vertical, and temporal coverage over vast oceans. Of special interest to hurricanes are microwave instruments onboard polar-orbiting operational environmental satellites that monitor the global atmosphere twice daily. Advanced Microwave Sounding Unit-A (AMSU-A) temperature sounders have been onboard U.S. National Oceanic and Atmospheric Administration (NOAA) polar-orbiting operational

environmental satellites NOAA-15 through NOAA-19 and the European Organization for the Exploitation of Meteorological Satellites MetOp-A/-B since 1998. Merrill (1995) and Brueske and Velden (2003) developed and tested an algorithm of retrieving tropical cyclone (TC) intensities from observations at a single AMSU channel. A regression algorithm to retrieve the warm-core of Hurricane Bonnie (1998) from AMSU-A temperature-sounding channels was developed and demonstrated by Zhu et al. (2002). Demuth et al. (2004), Knaff et al. (2004), and Demuth et al. (2006) used AMSU-A measurements to estimate the maximum sustained wind, minimum sea level pressure, and radii of winds of tropical cyclones. As a successor and combination of the AMSU-A and the microwave humidity sounder, the Advanced Technology Microwave Sounder (ATMS) onboard the Suomi National Polar-orbiting Partnership (S-NPP) satellite was successfully launched into a Sun-synchronous orbit on 28 October 2011 (Weng et al., 2012). The algorithm developed by Zhu et al. (2002) was applied to ATMS observations of Hurricane Sandy (2012) and a positive correlation between the maximum upper level warm anomaly and the maximum sustained winds was found (Zhu and Weng (2013). Due to scan biases found in the temperature retrievals obtained by the algorithm of Zhu et al. (2002) and Zhu and Weng (2013), Tian and Zou (2016) proposed four modifications to the temperature retrieval algorithm: (i) replace the simple scan correction term with regression coefficients that are explicit functions of scan position; (ii) use only a subset of ATMS temperature-sounding channels for retrieving the temperatures at certain pressure levels that are highly correlated (correlation coefficients greater than 0.5) to these channels; (iii) obtain regression coefficients using limb-corrected ATMS and collocated Global Positioning System (GPS) radio occultation (RO) observations in the month prior to the lifetime of the hurricane as training data sets; and (iv) obtain two sets of regression coefficients, one for clear-sky conditions and another for cloudy-sky conditions. The refined algorithm was applied to both AMSU-A and ATMS observations to demonstrate that the warm-core structures for Hurricanes Michael (2012) and Sandy (2012) during their lifetimes were more realistic than those obtained by both the unmodified algorithm and the even more advanced one-dimensional variational approach of the Microwave Integrated Retrieval System. Tian and Zou (2018) applied the temperature retrieval algorithm in Tian and Zou (2016) to microwave temperature sounders onboard four NOAA operational satellites to analyze the intensity variations in Hurricanes Harvey, Irma, and Maria (2017).

Although less contaminated by clouds and precipitation than infrared measurements (Chen et al., 2013; Hilton et al., 2012; Janssen, 1994; Le Marshall et al., 2006), microwave measurements for low- and middle-level temperature-sounding channels are still affected by optically thick and heavily precipitating clouds in hurricanes (Weng et al., 2003). As a result, in most TC cases populated with convection, only warm-cores in the upper troposphere can be derived from satellite microwave measurements. Cold temperature anomalies with extremely unrealistic magnitudes have appeared in all past warm-core retrieval results. Nonetheless, when the TC eye is sufficiently large such that significant portions of the eyewall are not in the FOV or the convection absent near the center, the warm-core can be resolved well into the middle troposphere channels. In this study, a remapping algorithm is introduced to reduce the random noise in ATMS observations and to make the fields of view (FOVs) the same size as AMSU-A FOVs (section 2). The regression coefficients for both clear-sky and cloudy conditions are obtained from GPS RO data and used as training data during the two-week period prior to the occurrence of a hurricane. After eliminating temperature-sounding channels with peak weighting functions (WFs) below 400 hPa in cloudy conditions, retrievals of warm-core structures are then made (section 3). The warm-core structures and their temporal evolutions during the lifetime of Hurricane Matthew (2016), the first Category 5 Atlantic hurricane since Hurricane Felix (2007), are retrieved from all available AMSU-A and ATMS observations and compared (section 4). Finally, a summary and conclusions are given in section 5.

2. Descriptions of ATMS Data and the Remapping Algorithm

2.1. ATMS and AMSU-A Data Characteristics

The ATMS and the AMSU-A provide measurements of atmospheric thermal emission in the microwave spectral region between 23 and 90 GHz. The ATMS is onboard the S-NPP satellite and the AMSU-A is onboard the NOAA-15, -18, -19, MetOp-A, and MetOp-B satellites. The ascending node of the S-NPP ATMS crosses the equator at 1:30 pm local time, that is, the local equator crossing time. For atmospheric temperature profile retrievals, ATMS channels 5–15 or AMSU-A channels 4–14 are used for hurricane warm-core retrievals. The peak WFs and center frequencies of these channels from the lowest to the highest channel number change from 850 hPa and 52.8 GHz to 2 hPa and 57.29 GHz, respectively. The antenna for ATMS channels 5–15 has a

Table 1
ATMS Channel Characteristics

Channel no.	Frequency (GHz)	Specification (K)	NEΔT (K)	Beam width (deg)	Peak WF (hPa)
1	23.8	0.5	0.25	5.2	Surface
2	31.4	0.6	0.3	5.2	Surface
3	50.3	0.7	0.35	2.2	Surface
4	51.76	0.5	0.28	2.2	950
5	52.8	0.5	0.25	2.2	850
6	53.596 ± 0.115	0.5	0.27	2.2	700
7	54.4	0.5	0.25	2.2	400
8	54.94	0.5	0.25	2.2	250
9	55.5	0.5	0.28	2.2	200
10	57.29	0.75	0.4	2.2	100
11	57.29 ± 0.217	1	0.53	2.2	50
12	57.29 ± 0.322 ± 0.048	1	0.55	2.2	25
13	57.29 ± 0.322 ± 0.022	1.25	0.82	2.2	10
14	57.29 ± 0.322 ± 0.010	2.2	1.13	2.2	5
15	57.29 ± 0.322 ± 0.0045	3.6	1.8	2.2	2
16	88.2	0.3	0.27	2.2	Surface
17	165.5	0.6	0.39	1.1	Surface
18	183.31 ± 7.0	0.8	0.35	1.1	800
19	183.31 ± 4.5	0.8	0.41	1.1	700
20	183.31 ± 3.0	0.8	0.48	1.1	500
21	183.31 ± 1.8	0.8	0.53	1.1	400
22	183.31 ± 1.0	0.9	0.68	1.1	300

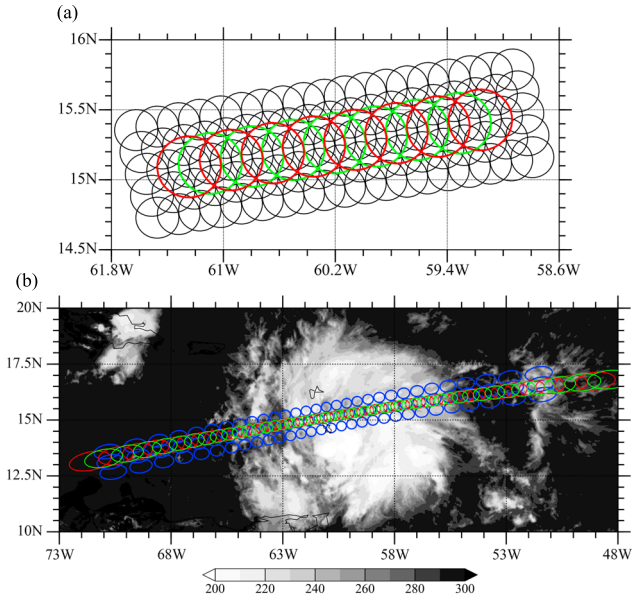

Figure 1. (a) Sizes of FOVs 40–56 for ATMS channels 5–15 over five consecutive scanlines (black circles) and the AMSU-A-like ATMS FOVs along the third scanline (nadir position at 15.25°N, 60.2°W) of the above five scanlines after remapping (red and green circles in turn for clarity) observed on 28 September 2016. (b) The 96 ATMS FOVs after remapping over the single scanline in (a) and the AMSU-A FOVs along the three consecutive scanlines from NOAA-18 (blue circles) that are near the ATMS scanline, overlapped onto GOES-13 imager channel 4 (10.7 μm) TB observations (unit K) at 1715 UTC 28 September 2016.

beam width of 2.2°, while that for AMSU-A channels 4–14 has a beam width of 3.3°. For the ATMS, the temperature-sounding channels (1–16) are kept in the same scan mode as the humidity-sounding channels (17–22) and with the same sampling time, a continuous-scan fashion is adopted. Therefore, 96 scene resolution cells are sampled at an interval of 8/3 s for each scan to cover 52.725° scan angles on both sides of the subsatellite path. The integration time for each FOV is 18 ms. By contrast, the AMSU-A scans the Earth scene within ±49.5° with respect to the nadir direction and has a total of 30 FOVs. There are significant overlaps among neighboring ATMS FOVs in both along-track and across-track directions but not for the AMSU-A. The swath width of the ATMS scan is 2,600 km, which is wider than its predecessor AMSU-A (2,343 km), and leaves almost no gaps near the equator, providing nearly full coverage of the low latitudes where hurricanes develop and intensify over the Atlantic and Pacific Oceans.

Random noise in measurements made by microwave temperature sounders AMSU-A and ATMS is estimated by standard deviations (Mo, 1996) and/or Allan deviations calculated from warm target measurements (Tian et al., 2015). These are known as the noise equivalent differential temperatures (NEDTs). The NEDTs of the ATMS channels are slightly higher than those of the corresponding AMSU-A channels because of the higher sampling rate of the ATMS, that is, a shorter effective integration time of each ATMS FOV (Weng et al., 2012). More detailed information of ATMS instrument characteristics is provided in Table 1.

2.2. A Remapping Algorithm and Results

A remapping algorithm developed by Atkinson (2011) is employed to convert the beam width of ATMS channels 5–15 to that of AMSU-A channels 4–14. The oversampling characteristics of ATMS observations make such

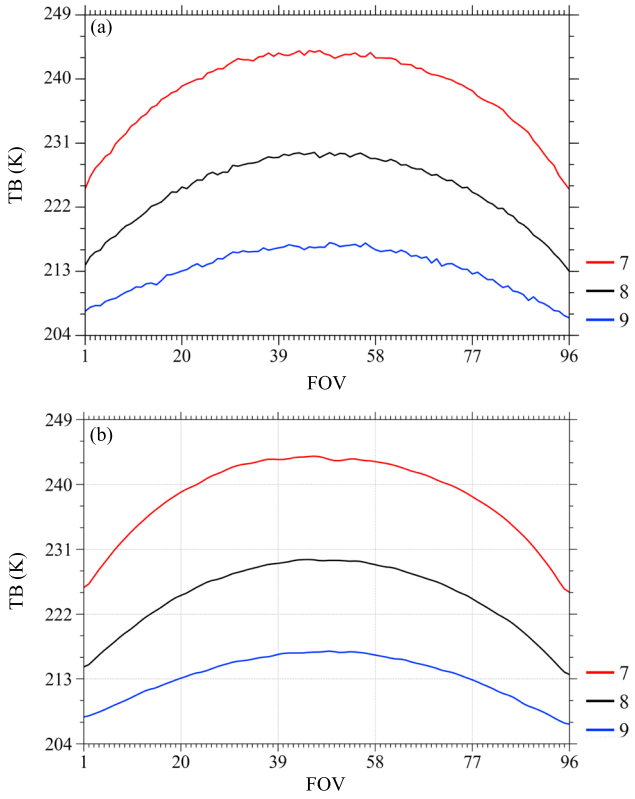

Figure 2. (a) ATMS channels 7 (red), 8 (black), and 9 (blue) TB observations along the same scanline as in Figure 1 on 28 September 2016. (b) Same as a except for after remapping.

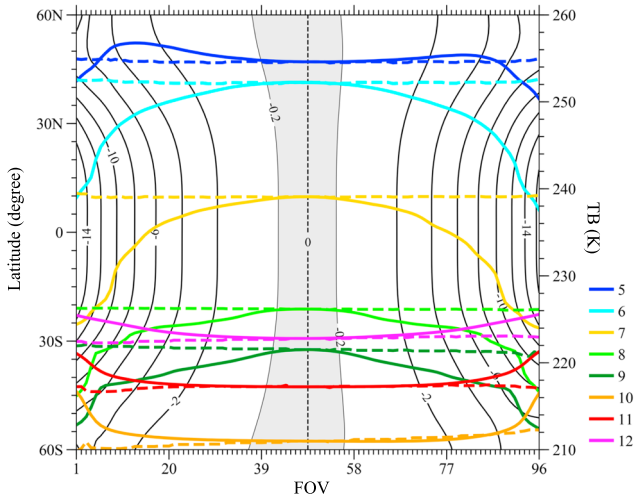

Figure 3. Limb-corrected values of ATMS channel 8 $[T_b^{Ch8}(i,j) - T_{b,LC}^{Ch8}(i,j)]$ TBs (black contour lines at 2-K intervals) as a function of scan position and latitude at 2° intervals, as well as scan variations in the global mean TBs $(\overline{T_b^{(m)}(i)})$ of channels 5–12 before (solid colored curves) and after (dashed colored curves) the limb correction. ATMS observations are from January and September of 2016.

a remap meaningful to produce AMSU-A-like ATMS observations. Having a consistent beam width between ATMS and AMSU-A is highly desirable because it allows the ATMS derived warm-cores be linked to AMSU-A derived ones that is required for several studies, such as examining the diurnal change of hurricane warm-cores and climate change (Yang & Zou, 2014).

Assuming the ATMS has a Gaussian beam, a modulation transfer function (*MTF*), defined as the spatial frequency response function of the 3-dB beam width (w), can be expressed as (Atkinson, 2011)

$$MTF_w(f) = \exp\left(-\frac{(\pi f w/2)^2}{\ln 2}\right), \quad (1)$$

where f is the spatial frequency and the reciprocal of the ATMS sampling distance (1.1°). The beam shape, called the point spread function, is the Fourier transform of *MTF* and can be written as

$$PSF_w(x) = \exp\left(-\left(\frac{x}{w/2}\right)^2 \ln 2\right). \quad (2)$$

The *MTF* of both the ATMS intrinsic beam width (w = 2.2°) and the targeted AMSU-A beam width (w = 3.3°) are first computed. The two-dimensional brightness temperatures (BTs) at any given ATMS temperature-sounding channel in the spatial domain $[T_b^{ATMS}(x,y)]$, where x and y represent the along-track and cross-track directions, respectively, are converted to the frequency domain $[F(\omega_x, \omega_x)]$ (Sorensen et al., 1987). The function $F(\omega_x, \omega_x)$ is then multiplied by the *MTF* modification factor $(MTF_{3.3°}^{AMSU-A}/MTF_{2.2°}^{ATMS})$ to obtain the *MTF* for the ATMS at the AMSU-A-like beam width:

$$MTF_{3.3°}^{AMSU-A\text{-like ATMS}} = F(\omega_x, \omega_y) MTF_{3.3°}^{AMSU-A}/MTF_{2.2°}^{ATMS}.$$

Finally, $MTF_{3.3°}^{AMSU-A\text{-like ATMS}}$ is converted back to the spatial domain to obtain AMSU-A-like ATMS BTs $[T_b^{AMSU-A\text{-like ATMS}}(x,y)]$ through the Fourier transform.

Figure 1a provides an illustration of the sizes of FOVs 40–56 for ATMS channels 5–15 over five consecutive scan lines and the AMSU-A-like ATMS FOVs along the third scan line of the above five scan lines after remapping observed on 28 September 2016. Note that the remapped FOVs are concentric to the original FOVs with larger sizes. Although the sizes of the AMSU-A-like ATMS FOVs generated by remapping are the same as those of the AMSU-A, the feature of the continuous-ATMS-scan fashion is kept, with 96 scene resolution cells covering 52.725° on both sides of the subsatellite path. In other words, ATMS observations still have much higher (~3 times) spatial samplings than AMSU-A observations after remapping. This is more clearly demonstrated in Figure 1b, which shows the ATMS FOVs after remapping over the single scan line seen in Figure 1a overlapped onto the AMSU-A FOVs along the three consecutive scan lines from NOAA-18 that are near the ATMS scan line. BT observations of channel 4 (10.7 μm) from the GOES-13 imager at 1715 coordinated universal time (UTC) 28 September 2016 are provided in Figure 1b to show the typical scales of clouds in a hurricane environment. The FOV sizes at large scan

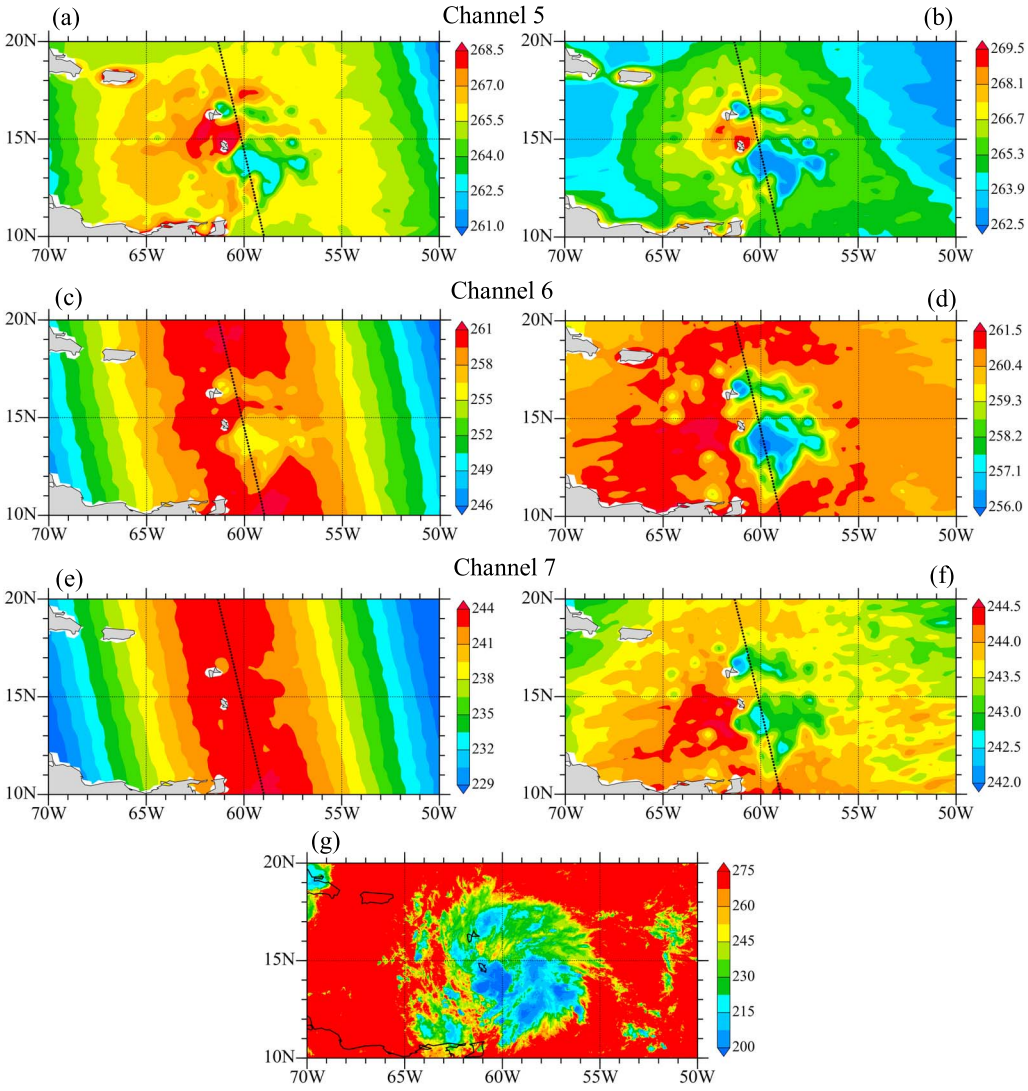

Figure 4. ATMS channels 5–7 TB observations (unit K) (left panels) before and (right panels) after the limb correction at 1716 UTC 28 September 2016. The black dotted lines show the nadir positions. (g) VIIRS infrared TB observations (10.7 um) at 1716 UTC 28 September 2016.

angles are much larger than those near nadir, especially in the cross-track direction. In other words, small-scale features of hurricanes, such as the eye, rainbands, and clear streaks between rainbands, are better resolved near the swath center than around swath edges. This point will be illustrated later (see section 4).

The remapping done to obtain AMSU-like ATMS observations involves a Gaussian weighted average of original ATMS observations in approximately nine ATMS FOVs. Therefore, the remapping will reduce the random noise of the observations. Figure 2 shows the cross-track variation in ATMS BT observations of channels 7, 8, and 9 along the same scan line shown in Figure 1 with its nadir position located at [15.25°N, 60.2°W] on 28 September 2016 before (Figure 2a) and after (Figure 2b) the remapping. As expected, the BT variations become smoother after the remapping for all three channels shown. Similar results are obtained for other channels and elsewhere (figures omitted). In fact, the noise reduction due to the remapping has significant impacts on warm-core retrieval results which will be shown later (see Figure 10 in section 4).

2.3. A Brief Description of Limb Correction and Rain Contamination

As a cross-track scanning radiometer, the ATMS receives atmospheric emissions from a larger scan angle to go over a longer optical path. Weather features could often be concealed in BTs by the prevailing scan

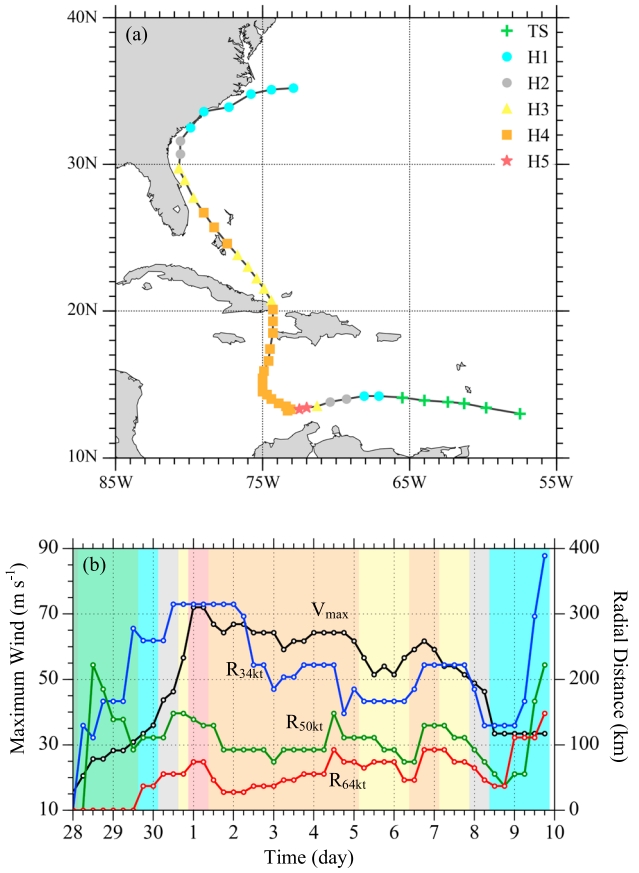

Figure 5. (a) The best track of Hurricane Matthew (2016) with the intensities marked in different colored shapes from 0000 UTC 28 September to 1800 UTC 9 October 2016 at 6-h intervals. (b) The maximum surface wind (black) and radii of 34- (blue), 50- (green), and 64-kt (red) winds from 28 September to 9 October 2016. The background colors show the intensity categories as defined in (a). TD, TS, and H1–H5 stand for tropical depression, tropical storm, and hurricane categories 1–5.

pattern. Goldberg et al. (2001) and Zhang et al. (2017) proposed a limb effect correction algorithm to remove the scan-dependent patterns in AMSU-A and ATMS BTs. The ATMS BTs after the limb correction ($T_{b,LC}^{(k)}$) are obtained as follows:

$$T_{b,LC}^{(k)}(i,j) = b_i^{(k)} + \sum_{m=k-1}^{k+1} a_i^{(m)} \left(T_b^{(m)}(i,j) - \overline{T_b^{(m)}}(i) \right), \quad (3)$$

where "*i*", "*j*", and "*k*" represent the scan position, scan line, and channel number, respectively; $T_b^{(k)}(i,j)$ is the BT of the k^{th} channel at the i^{th} scan position and the j^{th} scan line; $\overline{T_b^{(m)}}(i)$ is the global mean of BTs as a function of scan position *i*; and ($a_i^{(k-1)}$, $a_i^{(k)}$, and $a_i^{(k+1)}$) are the regression coefficients.

The regression coefficients are obtained by minimizing the following cost function:

$$J\left(a_i^{(k)}, b_i\right) = \sum_{\varphi} \left(T_{b,reg}^{(k)}(i,\varphi) - \overline{T_{b,nadir}^{(k)}(\varphi)} \right)^2, \quad (4)$$

where φ is the latitude and $T_{b,reg}^{(k)}(i,\varphi)$ is the regression function defined as

$$T_{b,reg}^{(k)}(i,\varphi) = b_i + \sum_{m=k-1}^{k+1} a_i^{(m)} \left[\overline{T_b^{(m)}(i,\varphi)} - \overline{T_b^{(m)}(i)} \right]. \quad (5)$$

The quantities $\overline{T_{b,nadir}^{(k)}(\varphi)}$ and $\overline{T_b^{(m)}(i,\varphi)}$ are the mean BTs in 2° latitudinal bands at the nadir (48th and 49th FOVs) and for different FOVs, respectively (Wark, 1993). For channels 5, 6, and 7, only observations over oceans are included in the calculations.

Global ATMS BT observations made in January and September of 2016 are used. The BTs at all scan angles are corrected with respect to the nadir position where the limb correction is zero. An example of the limb correction is provided in Figure 3 for ATMS channel 8, in which the differences in BT before [$T_b^{Ch8}(i,j)$] and after [$T_{b,LC}^{Ch8}(i,j)$] the correction are shown. The largest limb correction is at the largest scan angle near the equator (−14 K) and reduces to zero near the nadir (less than 0.2 K in magnitude for about 15 FOVs centered at the nadir). In Figure 3, we also show the scan variations in the global mean BTs of channels 5–12 before and after the limb correction. The scan variations of ATMS channels 5–9 (channels 10–12) are of a downward curving ("upward curving") shape as a result of a decrease (increase) in atmospheric temperature with increasing altitude in the troposphere (stratosphere). After the limb correction, the scan dependence of global mean BT observations for all temperature-sounding channels (5–12) employed in ATMS warm-core retrievals is successfully removed.

Hurricane Matthew around 1716 UTC 28 September 2016 is characterized by colder BTs (Figures 4b, 4d, and 4f) over cloudy regions based on Visible Infrared Imaging Radiometer Suite (VIIRS) BT observations at 10.7 μm (Figure 4g). A closer match between ATMS and VIIRS observations at small scales is not expected due to the much higher observational resolution of the VIIRS. The nadir FOV sizes of the ATMS and AMSU-A temperature-sounding channels (31.6 and 48.6 km, respectively) are much coarser than that of the VIIRS infrared channel at 10.7 μm (375 m).

Table 2
Data Count of RO Profiles Collocated With ATMS Observations From 1–27 September 2016

Satellite name	All sky	Clear sky
COSMIC	5,077	2,912
Metop-A	3,438	1,943
Metop-B	4,021	2,363
Total	12,536	7,218 (58%)

3. ATMS Temperature Retrieval Algorithm for Hurricane Matthew

3.1. Case Description

Hurricane Matthew (2016) was the first Atlantic hurricane that reached category 5 intensity since Hurricane Felix in 2007. Figure 5 provides the

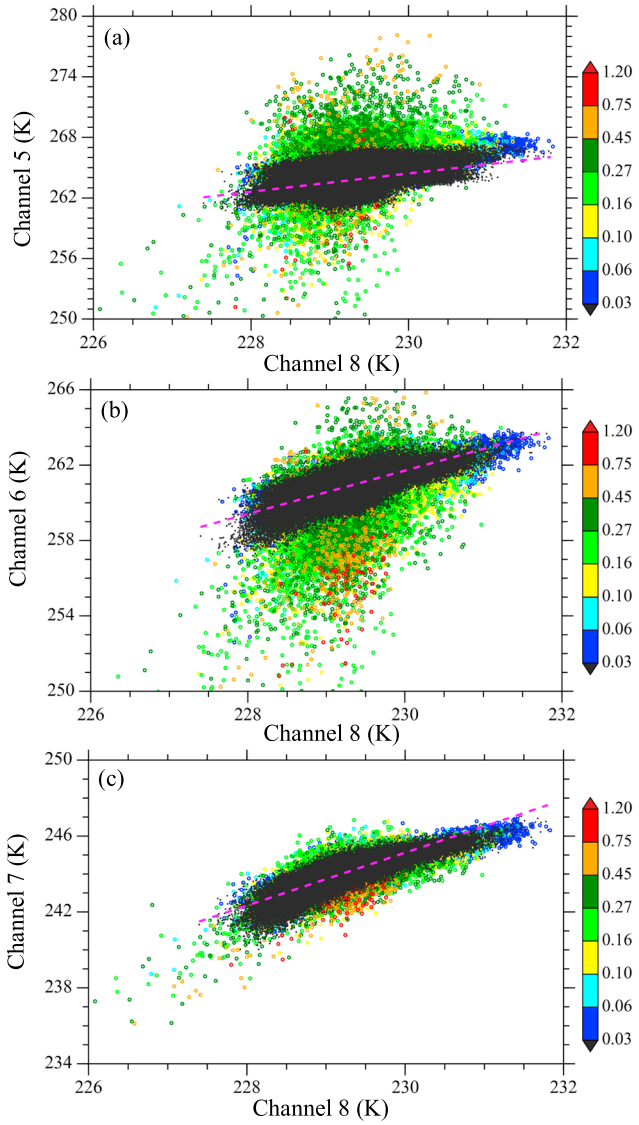

Figure 6. Scatterplots of ATMS TB observations (limb corrected) on 28 September 2016 within 10°N–20°N between (a) channels 5 and 7, (b) channels 6 and 8, and (c) channels 7 and 8. The colors show LWP values. The magenta lines are linear regression best fit lines for clear-sky data (black dots; LWP $<$ 0.03 g/kg).

6-hourly best track (Figure 5a), the maximum surface wind as well as the radii of the 34-, 50-, and 64-kt winds (Figure 5b), and the intensity category of Hurricane Matthew from 0000 UTC 28 September 2016 to 1800 UTC 9 October 2016. Hurricane Matthew was a tropical storm on 28 September, intensified to a category-1 hurricane on 29 September, and quickly reached category-5 intensity the next day. It soon turned from moving westward to northward, weakened gradually, passed Cuba, and moved along and off the east coasts of Florida and Georgia. Matthew made its landfall in South Carolina on 7 October 2016 as a category-1 hurricane, immediately drifted away from land, and moved eastward into the ocean again. Hurricane Matthew had catastrophic consequences, including hundreds of deaths and billions of dollars of economic losses in five affected countries.

3.2. A Brief Description of the Warm-Core Retrieval Algorithm

In order to examine the warm-core structures of Hurricane Matthew, the three-dimensional atmospheric temperature fields during the life cycle of Matthew are first retrieved from the remapped and limb-corrected ATMS BT observations. Specifically, the atmospheric temperatures at different pressure levels

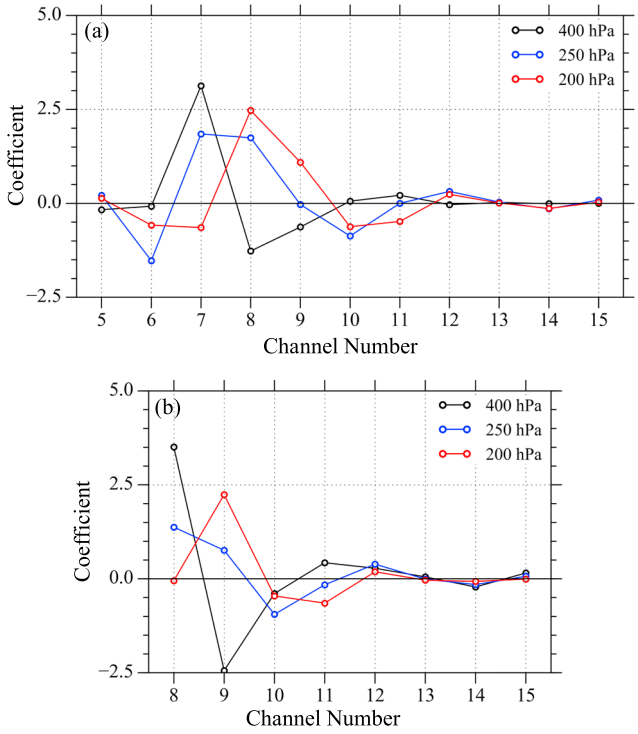

Figure 7. Regression coefficients for ATMS temperature retrievals at 400 (black), 250 (blue), and 200 hPa (red) trained with collocated RO data during the period 1–27 September 2016 in (a) clear-sky and (b) cloudy conditions. The intercepts for temperature retrievals at 400, 250, and 200 hPa are −67.78, 156.70, and −112.72 for clear-sky conditions and −85.95, −83.30, and −39.11 for cloudy conditions.

are expressed as functions of ATMS BT observations at each ATMS/AMSU-A FOV location by the following equation:

$$T(p) = C_0(p) + \sum_{i=i_{1,p}}^{i_{2,p}} C_i(p) T_{b,i}(p), \tag{6}$$

where p is pressure and $(i_{1,\ p}, i_{1,\ p}+1, i_{1,\ p}+2, \cdots, i_{2,\ p})$ represents a subset of AMSU-A channels 4–14 (ATMS channels 5–15) that are correlated with the atmospheric temperatures at the pressure level p (Tian & Zou, 2016). Equation (6) is similar to the refined temperature retrieval algorithm proposed by Tian and Zou (2016) except for removing the scan-angle dependence of the regression coefficients. In order to remove rain contamination from the retrieved atmospheric temperatures in the lower troposphere, ATMS channel 5–7 and AMSU-A channels 4–6 are not used in cloudy conditions. The regression coefficients (C_0 and C_i) are obtained from a training data set, namely, ATMS observations over the ocean and collocated GPS RO temperature profiles from 1 to 27 September 2016. Data are collocated if they fall within a 3-h time window and a 100-km spatial distance. The total number of RO profiles collocated with ATMS observations from the Constellation Observing System for Meteorology, Ionosphere, and Climate (COSMIC), MetOp-A, and MetOp-B satellites between 60°S and 60°N are provided in Table 2. Out of the 12,536 RO profiles that are collocated with ATMS data, 58% represent clear-sky conditions (liquid water path (LWP) $<$ 0.03 g/kg).

Figure 6 shows scatterplots of ATMS BT observations after limb correction on 28 September 2016 within [10°N–20°N], that is, channel 5 versus channel 8 (Figure 6a), channel 6 versus channel 8 (Figure 6b), and channel 7 versus channel 8 (Figure 6c). The values of LWP for cloudy (LWP $\geq$ 0.03 g/kg) and clear-sky (LWP $<$ 0.03 g/kg) observations are shown as colored and black dots, respectively. Three corresponding linear regression functions are derived from clear-sky data. Cloud contamination is seen in the three low-level ATMS channels (5–7). BTs are either elevated or lowered in the presence of clouds more significantly for the lower-level channels 5 and 6, and less for channel 7. In most TC cases, cloud contamination in ATMS channel 8 is negligible. But for some small-cored, intense convection TCs, cloud contamination in ATMS channel 8 might be more significant.

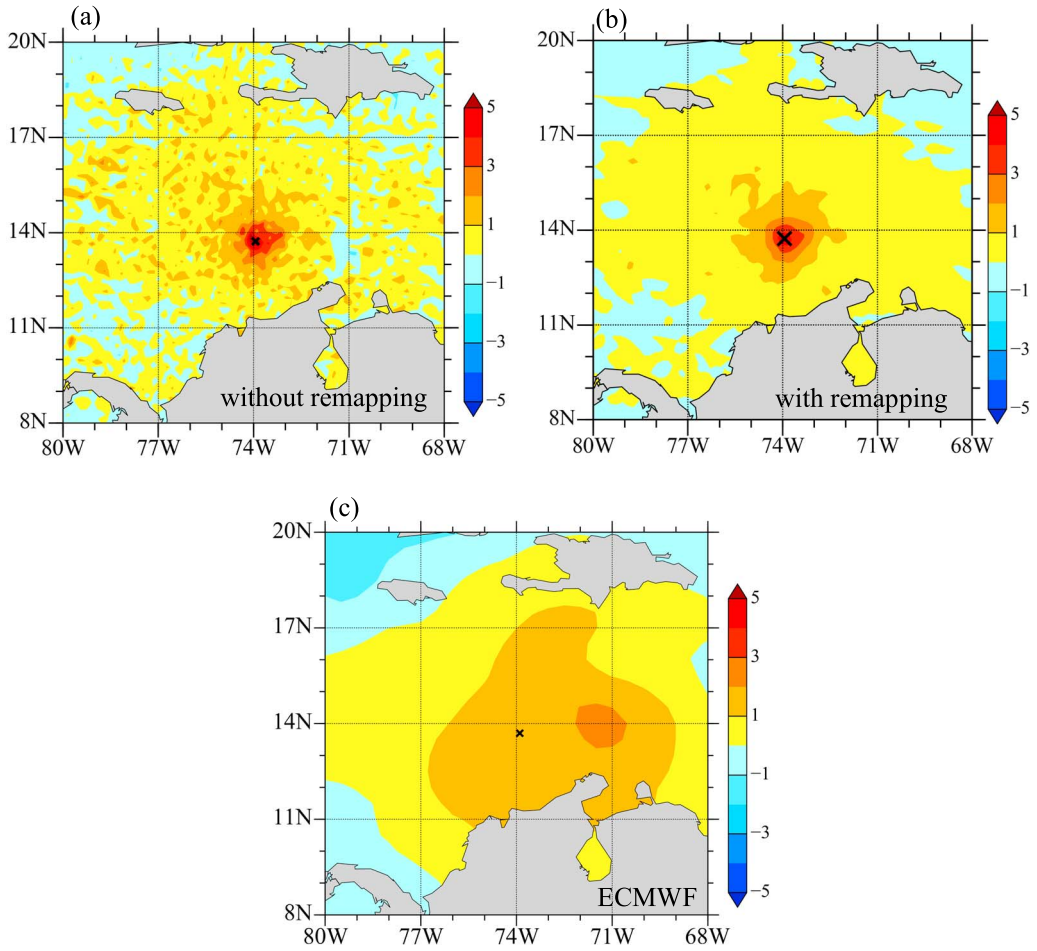

Figure 8. Temperature anomalies at 250 hPa at 0643 UTC 2 October 2016 calculated from ATMS observations (a) without and (b) with remapping. (c) Temperature anomalies calculated with ECMWF interim reanalysis data. The black cross shows the location of the observed hurricane center.

The regression coefficients for retrieving atmospheric temperatures at the 400-, 250-, and 200-hPa pressure levels are provided in Figure 7. The 400-, 250-, and 200-hPa pressure levels are where the WF peaks of channels 7, 8, and 9, respectively, are located. The regression coefficients are the largest for the channel with its WF peak located at the same 400-, 250-, and 200-hPa pressure levels, respectively, except for channel 8 in cloudy conditions. In clear-sky conditions (Figure 7a), channels 6, 8, and 9 also contribute to the temperature retrieval at 400 hPa (channel 7's WF peak); channels 6, 7, 9, and 10 contribute to the temperature retrieval at 250 hPa (channel 8's WF peak); and channels 6, 7, 9, 10, and 11 contribute to the temperature retrieval at 200 hPa (channel 9's WF peak). Channels whose WF peaks are further away from the pressure level on which the temperature is to be retrieved have little impact on the retrieval. The variations in the magnitudes of the regression coefficients in cloudy conditions are similar for temperature retrievals at the 250- and 200-hPa pressure levels (Figure 7b). Since channel 7 is not used in cloudy conditions, the regression coefficients for channel 8 are the largest for temperature retrievals at 400 hPa.

4. Numerical Results of Matthew's Warm-Core Structures and Evolutions

Temperature anomalies at 250 hPa on 0600 UTC 2 October 2016 calculated from ATMS BT observations without and with remapping are presented in Figures 8a and 8b, respectively. Here the temperature anomalies are calculated by subtracting the mean temperature averaged within a 15° latitude/longitude box centered at the storm center but outside of the 34-knot wind radius circle. The temperature retrieval without applying the remapping algorithm (Figure 8a) contains significant noise (~1 K), which is successfully mitigated by the

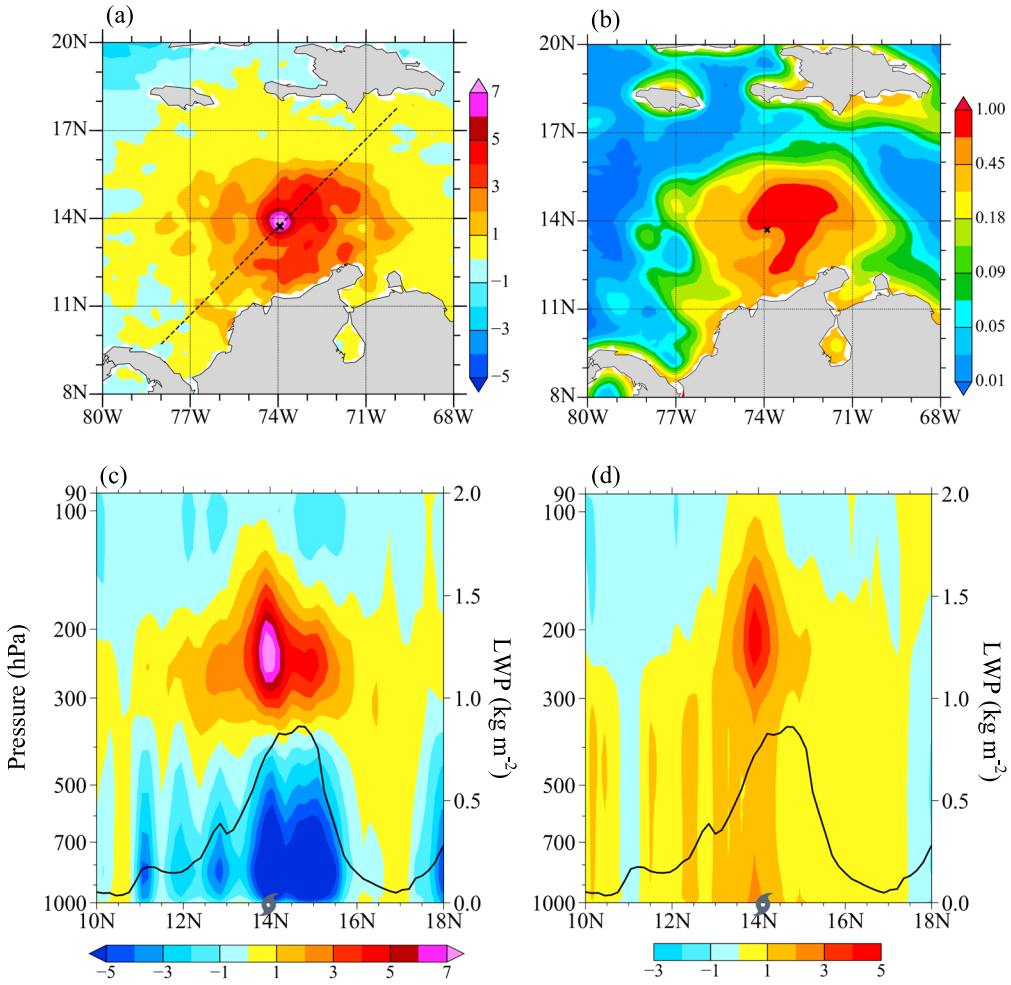

Figure 9. (a) Temperature anomalies at 250 hPa (unit K), (b) liquid water path (unit kg/m^2), and (c) the vertical cross section of temperature anomalies following the dashed line in a at 0634 UTC 2 October 2016 obtained from remapped ATMS TB observations without eliminating channels 5, 6, and 7. The regression is made using data representing cloudy conditions. (d) Same as (c) except for results obtained from remapped ATMS TB observations with channels 5, 6, and 7 eliminated in cloudy conditions. (e and f) Same as (c) except for results from (e) the ECMWF interim reanalysis at 0600 UTC and (f) the MIRS retrievals at 0634 UTC 2 October 2016.

remapping algorithm (Figure 8b). The warm-core center of Hurricane Matthew has a temperature anomaly of about 5 K and is centered at the observed hurricane location. The warm-core in the European Centre for Medium-Range Weather Forecasts (ECMWF) ERA-interim temperature analysis (Figure 8c) is misplaced to the east by more than 2 degrees of longitude, and is too broad and too weak, which is existent in global large-scale analyses (Dee et al., 2011).

The impact of rain contamination on the warm-core retrieval obtained without eliminating channels 5, 6, and 7 for the regression in cloudy conditions is shown in Figure 9. The temperature anomalies at 250 hPa (Figure 9a) contain a rainband structure that is in phase with the LWP distribution at 0600 UTC 2 October 2016 (Figure 9b). The maximum temperature anomaly at the warm-core center (Figure 9a) is more than 3 K higher than that in Figure 8b. The vertical cross section of the temperature anomalies (Figure 9c) shows a series of cold anomalies in the lower troposphere, with larger magnitudes over areas with stronger LWPs. Such unrealistic cold anomalies below the upper-level warm-core is not seen in the retrieval that neglects channels 5, 6, and 7 in cloudy conditions (Figure 9d) nor in the ECMWF interim reanalysis (Figure 9e). It should also be pointed out that the warm-core intensity around 250 hPa becomes stronger due to rain contaminations on channels 5–7 (Figure 9c). The observed brightness temperatures of channels 5 and 6 are lower in the presence of rain due to scattering effects

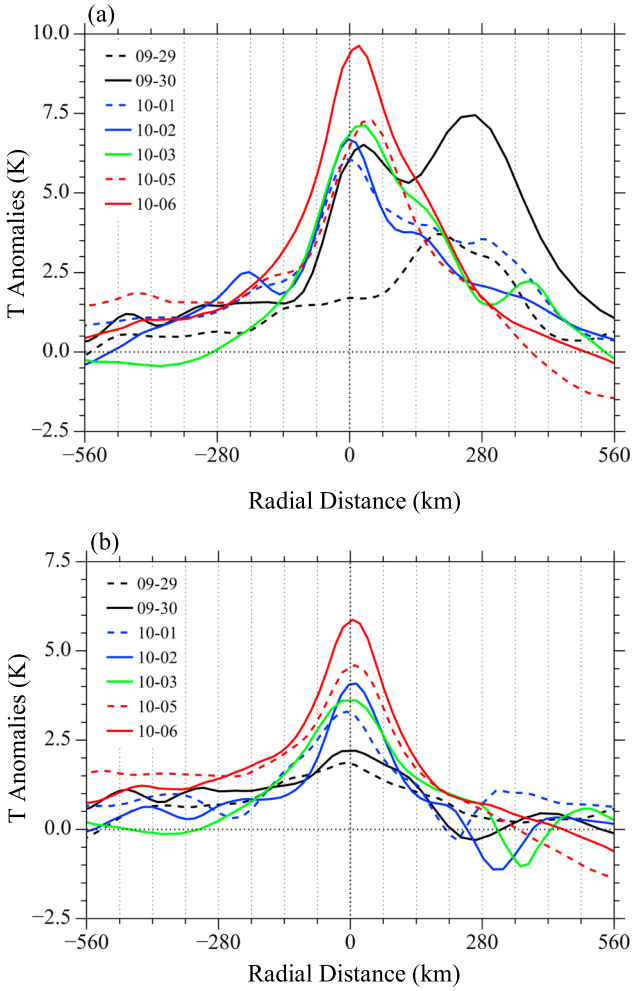

Figure 10. ATMS-derived temperature anomalies at 250 hPa as a function of distance from the center of Hurricane Matthew in the direction from west to east during the period 30 September 30 to 9 October 2016 calculated (a) without and (b) with remapping and the elimination of channels 5, 6, and 7 for the regression in cloudy conditions. The solid and dashed colored lines are for different days.

(Figure 6), and their correlations with the upper tropospheric (200 and 250 hPa) atmospheric temperatures are negative (Tian & Zou, 2016). When channel 6 is included, the retrieved atmospheric temperatures in the upper troposphere were elevated due to a negative regression coefficient (Figure 7a) and lower brightness temperatures. Impacts of channel 5 on the temperature retrieval are small since the regression coefficient for channel 5 is near zero (see Figure 7a). The temperature anomaly obtained from the Microwave Integrated Retrieval System (Figure 9f) also displays a warm-core around 200 hPa. An extremely warm center (>7 K) peaking near the surface and small horizontal-scale oscillating features are found in the Microwave Integrated Retrieval System results, both of which seem not physical. The ATMS-derived warm-core is much more compact and located at a higher altitude than that in the ECMWF reanalysis. The maximum LWP from ATMS is located to the northeast of the warm-core and hurricane center.

The radial profiles of ATMS-derived temperature anomalies from 30 September to 9 October 2016 are shown in Figure 10a (without averaging) and Figure 10b (with averaging, and with exclusion of channels 5, 6, and 7 in cloudy conditions). The modified hurricane warm-core retrieval algorithm for ATMS observations gives more compact warm-core structures and more consistent temporal evolutions.

The temporal evolution of the warm-core at 250 hPa is provided during the time period from 0134 local standard time 2 October to 0115 local standard time 3 October 2016 based on AMSU-A observations from

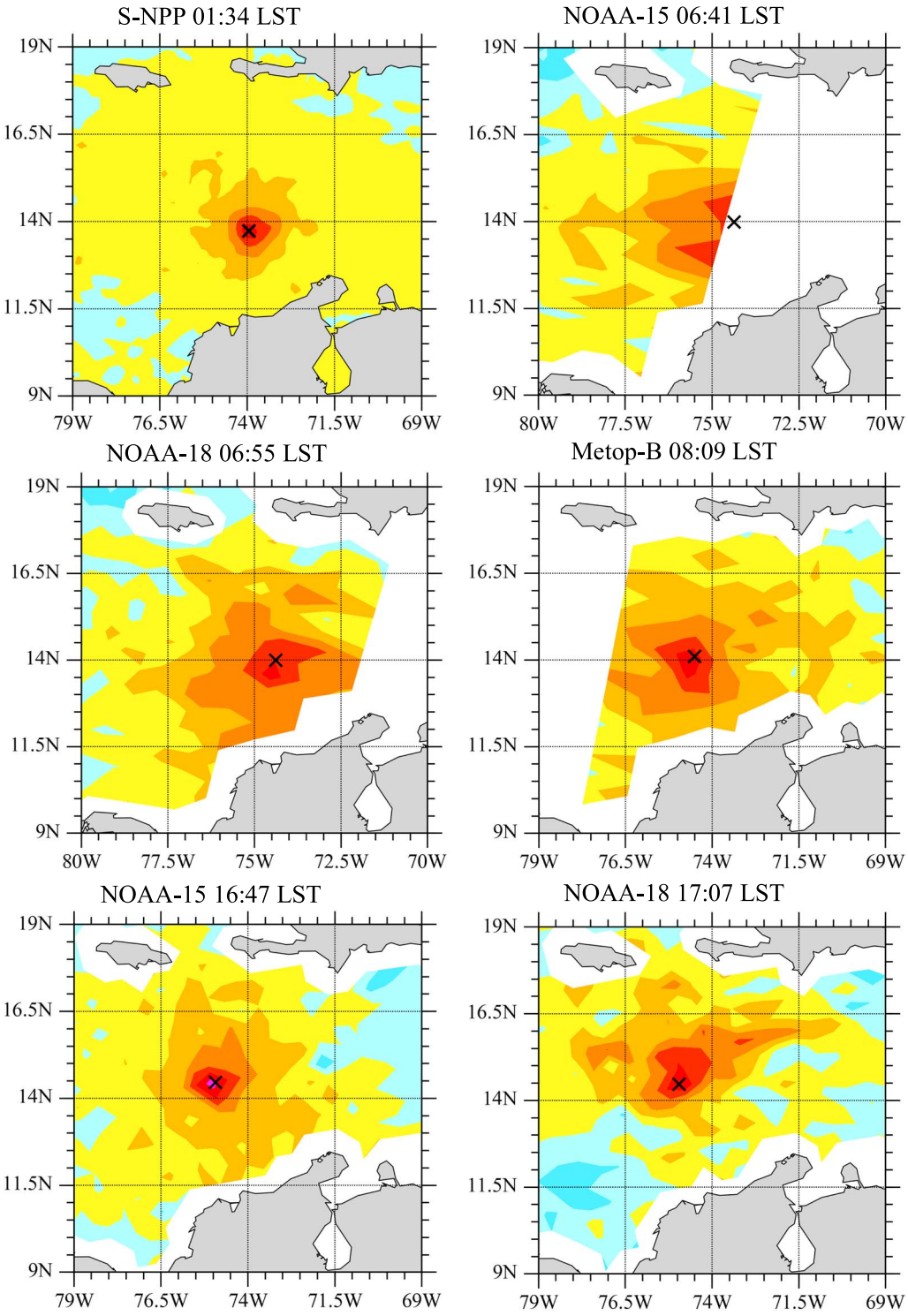

Figure 11. Hurricane Matthew's warm-core temperature anomaly structures at 250 hPa (unit K) on and between 0134 local standard time (LST) 2 October to 1756 LST 3 October 2016 retrieved from Metop-B, NOAA-15, and NOAA-18 AMSU-A and S-NPP ATMS observations. The LSTs and satellite names are indicated above each panel.

Metop-B, NOAA-15, and NOAA-18, and S-NPP ATMS observations (Figure 11). NOAA-19 AMSU-A observations are not used since the NEDTs for channels 7 and 8 are far above the specifications. Warm-core structures and intensities vary with time. The warm-cores near the nadir (the swath middle)

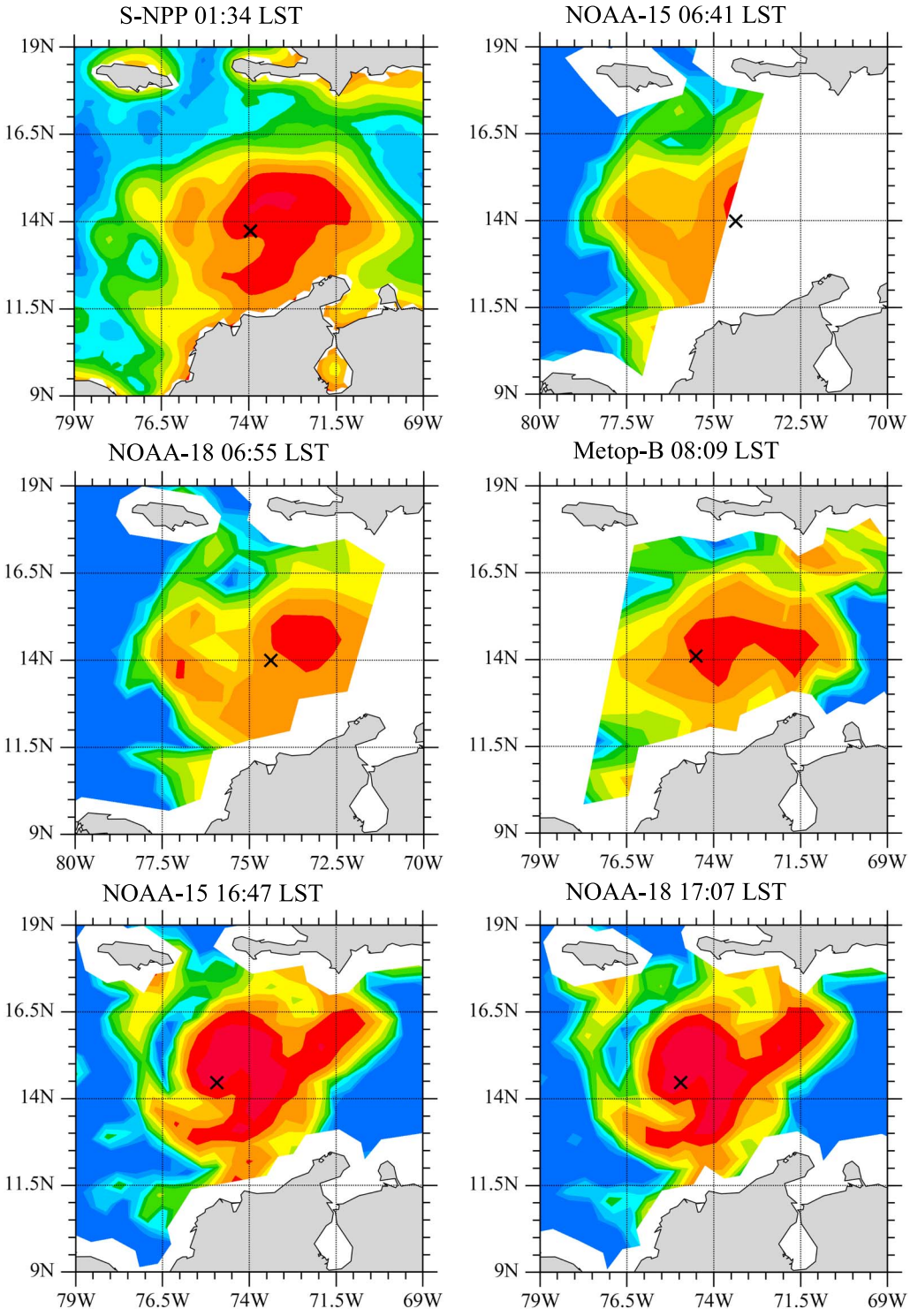

Figure 12. Same as Figure 11 except for LWP.

are generally smaller than those near the swath edges, which are a result of the scan dependence of the observational resolution. AMSU-A-derived warm-cores are larger than those from the ATMS due to the coarser observational sampling of the AMSU-A. Also, the maximum of the warm anomaly is located at exactly the best-track hurricane center, suggesting that Hurricane Matthew maintained a straight vertical structure during this time period. The strongest warm-core intensity is observed at 1647 UTC 2

October by NOAA-15 AMSU-A. It agrees with what was reported by Stewart (2017) that Hurricane Matthew underwent an intensification period on 2 October and reached a peak intensity on the same day later. Similar to Figures 9a and 9b, it is further confirmed that the temperature anomalies in the upper troposphere at all times shown in Figure 11 do not have rainband-like structures that are in phase with the LWP distribution at the corresponding times (Figure 12).

5. Summary and Conclusions

ATMS BT observations have random noise with relatively large magnitudes that obscures the ATMS-retrieved atmospheric temperature fields. A remapping algorithm is applied to ATMS observations to reduce their random noise. Even though the impact of this noise on ATMS warm-core retrievals is eliminated after applying the remapping algorithm to ATMS observations, an unrealistic rainband-like warm-anomaly structure is found in hurricane rainband areas. This is caused by cloud contamination on ATMS channels 5, 6, and 7 (AMSU-A channels 4, 5, and 6). The elimination of these channels for ATMS/AMSU-A temperature retrievals in cloudy conditions avoids not only the unrealistic rainband-like warm anomaly but also the unrealistic cold anomalies in the lower troposphere. A limb correction is finally applied to ATMS and AMSU-A observations so that there are enough GPS RO data collocated with AMSU-A/ATMS data to serve as a training data set.

The 3-D temperature anomaly fields during the life cycle of Hurricane Matthew (2016) are then retrieved using the same temperature retrieval algorithm as that developed by Tian and Zou (2016) except for the above-mentioned three changes. Compared with the temperature anomalies from the ECMWF interim reanalysis, the warm-core structures retrieved from ATMS observations are much more compact and closer to the best-track positions. The unrealistic rainband-like warm-core structures that are seen in the temperature retrieval from the remapped ATMS BT observations, which are in phase with the rainbands revealed by the VIIRS 10.8-μm radiance observations, are mostly eliminated. It is finally shown that AMSU-A observations from Metop-B, NOAA-15, and NOAA-18, and S-NPP ATMS observations together illustrate the temporal evolution of the warm-core at ~1.5-h intervals.

It may be possible to observe a better-than-hourly evolution of hurricane warm-cores during the 2018 hurricane season since NOAA-20 ATMS observations are now available. The warm-core results, along with microwave-imager-retrieved total precipitable water, surface wind speed, and sea surface temperature, as well as S-NPP and NOAA-20 Ozone Mapping and Profile Suite total column ozone, will be incorporated into a new satellite-observation-based vortex initialization as a follow-on study.

Acknowledgments
This study was supported by NOAA grant NA14NES4320003 (Cooperative Institute for Climate and Satellites (CICS)) at the University of Maryland/ESSIC. The ATMS and VIIRS observations employed in this study were obtained from NOAA's Comprehensive Large Array-data Stewardship System at the website http://www.class.ncdc.noaa.gov/saa/products/welcome, and ECMWF ERA-Interim Reanalysis data were obtained from the website at http://www.ecmwf.int/en/research/climate-reanalysis/era-interim. Results used to generate the figures in this study are available at http://jlrdata.umd.edu/Tianshare/HurricaneMatthew.html.

References

Atkinson, N. (2011). Annex to AAPP scientific documentation: pre-processing of ATMS and CrIS. *Document* (NWPSAF-MO-UD-027).

Brueske, K. F., & Velden, C. S. (2003). Satellite-based tropical cyclone intensity estimation using the NOAA-KLM series advanced microwave sounding unit (AMSU). *Monthly Weather Review*, *131*(4), 687–697. https://doi.org/10.1175/1520-0493(2003)131<0687:SBTCIE>2.0.CO;2

Chen, H., & Zhang, D.-L. (2013). On the rapid intensification of Hurricane Wilma (2005). Part II: Convective bursts and the upper-level warm core. *Journal of the Atmospheric Sciences*, *70*(1), 146–162.

Chen, Y., Han, Y., & Weng, F. (2013). Detection of Earth-rotation Doppler shift from Suomi national polar-orbiting partnership cross-track infrared sounder. *Applied Optics*, *52*(25), 6250–6257. https://doi.org/10.1364/AO.52.006250

Dee, D. P., Uppala, S. M., Simmons, A. J., Berrisford, P., Poli, P., Kobayashi, S., et al. (2011). The ERA-interim reanalysis: Configuration and performance of the data assimilation system. *Quarterly Journal of the Royal Meteorological Society*, *137*(656), 553–597. https://doi.org/10.1002/qj.828

Demuth, J. L., DeMaria, M., & Knaff, J. A. (2006). Improvement of advanced microwave sounding unit tropical cyclone intensity and size estimation algorithms. *Journal of Applied Meteorology and Climatology*, *45*(11), 1573–1581. https://doi.org/10.1175/JAM2429.1

Demuth, J. L., DeMaria, M., Knaff, J. A., & Vonder Haar, T. H. (2004). Evaluation of advanced microwave sounding unit tropical-cyclone intensity and size estimation algorithms. *Journal of Applied Meteorology and Climatology*, *43*(2), 282–296. https://doi.org/10.1175/1520-0450(2004)043<0282:EOAMSU>2.0.CO;2

Dolling, K., & Barnes, G. M. (2012). Warm-core formation in tropical storm Humberto (2001). *Monthly Weather Review*, *140*(4), 1177–1190.

Durden, S. L. (2013). Observed tropical cyclone eye thermal anomaly profiles extending above 300 hPa. *Monthly Weather Review*, *141*(12), 4256–4268. https://doi.org/10.1175/MWR-D-13-00021.1

Goldberg, M. D., Crosby, D. S., & Zhou, L. (2001). The limb adjustment of AMSU-A observations: Methodology and validation. *Journal of Applied Meteorology and Climatology*, *40*(1), 70–83.

Halverson, J. B., Simpson, J., Heymsfield, G., Pierce, H., Hock, T., & Ritchie, L. (2006). Warm core structure of hurricane Erin diagnosed from high altitude dropsondes during CAMEX-4. *Journal of the Atmospheric Sciences*, *63*(1), 309–324. https://doi.org/10.1175/JAS3596.1

Hawking, H. F., & Rubsam, D. T. (1968). Hurricane Hilda, 1964. II, structure and budgets of the hurricane on October J 1964. *Monthly Weather Review*, *96*(9), 617–636. https://doi.org/10.1175/1520-0493(1968)096<0617:HH>2.0.CO;2

Hawkins, H. F., & Imbembo, S. M. (1976). The structure of a small, intense hurricane—Inez 1966. *Monthly Weather Review*, *104*(4), 418–442. https://doi.org/10.1175/1520-0493(1976)104<0418:TSOASI>2.0.CO;2

Hilton, F., Armante, R., August, T., Barnet, C., Bouchard, A., Camy-Peyret, C., et al. (2012). Hyperspectral Earth observation from IASI: Five years of accomplishments. *Bulletin of the American Meteorological Society*, *93*(3), 347–370. https://doi.org/10.1175/BAMS-D-11-00027.1

Janssen, M. A. (1994). Atmospheric remote sensing by microwave radiometry. *International Journal of Climatology*, *14*(9), 1062–1063.
Knaff, J. A., Seseske, S. A., DeMaria, M., & Demuth, J. L. (2004). On the influences of vertical wind shear on symmetric tropical cyclone structure derived from AMSU. *Monthly Weather Review*, *132*(10), 2503–2510. https://doi.org/10.1175/1520-0493(2004)132<2503:OTIOVW>2.0.CO;2
Komaromi, W. A., & Doyle, J. D. (2017). Tropical Cyclone Outflow and Warm Core Structure as Revealed by HS3 Dropsonde Data. *Monthly Weather Review*, *145*(4), 1339–1359.
La Seur, N. E., & Hawkins, H. F. (1963). An analysis of hurricane Cleo (1958) based on data from research reconnaissance aircraft. *Monthly Weather Review*, *91*(10), 694–709. https://doi.org/10.1175/1520-0493(1963)091<0694:AAOHCB>2.3.CO;2
Le Marshall, J., Jung, J., Derber, J., Chahine, M., Treadon, R., Lord, S. J., et al. (2006). Improving global analysis and forecasting with AIRS. *Bulletin of the American Meteorological Society*, *87*(7), 891–895. https://doi.org/10.1175/BAMS-87-7-891
Merrill, R. T. (1995). Simulations of physical retrieval of tropical cyclone thermal structure using 55-GHz band passive microwave observations from polar-orbiting satellites. *Journal of Applied Meteorology*, *34*(4), 773–787. https://doi.org/10.1175/1520-0450(1995)034<0773:SOPROT>2.0.CO;2
Mo, T. (1996). Prelaunch calibration of the advanced microwave sounding unit-A for NOAA-K. *IEEE Transactions on Microwave Theory and Techniques*, *44*(8), 1460–1469.
Sorensen, H. V., Jones, D., Heideman, M., & Burrus, C. (1987). Real-valued fast Fourier transform algorithms. *IEEE Transactions on Acoustics, Speech, and Signal Processing*, *35*(6), 849–863.
Stern, D. P., & Nolan, D. S. (2012). On the height of the warm core in tropical cyclones. *Journal of the Atmospheric Sciences*, *69*(5), 165–1680.
Stewart, S. R., 2017: Tropical cyclone report: Hurricane Matthew (AL142016). 7 April 2016, 96 pp., http://www.nhc.noaa.gov/data/tcr/AL142016_Matthew.pdf.
Tian, X., & Zou, X. (2018). Capturing Size and Intensity Changes of Hurricanes Irma and Maria (2017) from Polar-Orbiting Satellite Microwave Radiometers. *Journal of Atmospheric Sciences*, *75*(8), 2509–2522.
Tian, X., & Zou, X. (2016). ATMS- and AMSU-A-derived hurricane warm core structures using a modified retrieval algorithm. *Journal of Geophysical Research*, *121*.
Tian, M., Zou, X., & Weng, F. (2015). Use of Allan Deviation for Characterizing Satellite Microwave Sounder Noise Equivalent Differential Temperature (NEDT). *Ieee Geoscience and Remote Sensing Letters*, *12*(12), 2477–2480.
Wark, D. Q. (1993). Adjustment of TIROS Operational Vertical Sounder data to a vertical view (NOAA Tech. Rep. NESDIS-64, 36 pp).
Weng, F., Zhao, L., Ferraro, R. R., Poe, G., Li, X., & Grody, N. C. (2003). Advanced microwave sounding unit cloud and precipitation algorithms. *Radio Science*, *38*(4), 8068. https://doi.org/10.1029/2002RS002679
Weng, F., Zou, X., Wang, X., Yang, S., & Goldberg, M. (2012). Introduction to Suomi NPP ATMS for NWP and tropical cyclone applications. *Journal of Geophysical Research*, *117*, D19112. https://doi.org/10.1029/2012JD018144
Yang, H., & Zou, X. (2014). Optimal ATMS remapping algorithm for climate research. *IEEE Transactions on Geoscience and Remote Sensing*, *52*(11), 7290–7296.
Zhang, K., Zhou, L., Goldberg, M., Liu, X., Wolf, W., Tan, C., & Liu, Q. (2017). A Methodology to Adjust ATMS Observations for Limb Effect and Its Applications. *Journal of Geophysical Research*, *122*(21), 11,347–11,356.
Zhu, T., & Weng, F. (2013). Hurricane Sandy warm-core structure observed from advanced technology microwave sounder. *Geophysical Research Letters*, *40*, 3325–3330. https://doi.org/10.1002/grl.50626
Zhu, T., Zhang, D.-L., & Weng, F. (2002). Impact of the advanced microwave sounding unit measurements on hurricane prediction. *Monthly Weather Review*, *130*(10), 2416–2432. https://doi.org/10.1175/1520-0493(2002)130<2416:IOTAMS>2.0.CO;2